

Testing adiabatic contraction with SDSS elliptical galaxies

A.E. Schulz^{1*}, Rachel Mandelbaum², Nikhil Padmanabhan³

¹*Institute for Advanced Study, Einstein Drive, Princeton NJ 08540, USA*

²*Department of Astrophysical Sciences, Princeton University, Peyton Hall, Princeton, NJ 08544, USA*

³*Department of Physics, Yale University, New Haven, CT 06511*

13 February 2022

ABSTRACT

We study the profiles of 75 086 elliptical galaxies from the Sloan Digital Sky Survey (SDSS) at both large ($70 - 700 h_{70}^{-1} \text{kpc}$) and small ($\sim 4 h_{70}^{-1} \text{kpc}$) scales. Weak lensing observations in the outskirts of the halo are combined with measurements of the stellar velocity dispersion in the interior regions of the galaxy for stacked galaxy samples. The weak lensing measurements are well characterized by a Navarro, Frenk and White (NFW) profile. The dynamical mass measurements exceed the extrapolated NFW profile even after the estimated stellar masses are subtracted, providing evidence for the modification of the dark matter profile by the baryons. This excess mass is quantitatively consistent with the predictions of the adiabatic contraction (AC) hypothesis. Our finding suggests that the effects of AC during galaxy formation are stable to subsequent bombardment from major and minor mergers. We explore several theoretical and observational systematics and conclude that they cannot account for the inferred mass excess. The most significant source of systematic error is in the IMF, which would have to increase the stellar mass estimates by a factor of two relative to the Kroupa IMF to fully explain the mass excess without AC, causing tension with results from SAURON (Cappellari et al. 2006). We demonstrate a connection between the level of contraction of the dark matter halo profile and scatter in the size luminosity relation, which is a projection of the fundamental plane. Whether or not AC is the mechanism supplying the excess mass, models of galaxy formation and evolution must reconcile the observed halo masses from weak lensing with the comparatively large dynamical masses at the half light radii of the galaxies.

Key words: cosmology: observations — gravitational lensing — dark matter — galaxies: clusters: general

1 INTRODUCTION

In hierarchical models of structure formation, matter organizes itself into gravitationally bound halos that are formed through mergers of smaller halos, and by accretion along filamentary large scale structure. The properties of these halos have been studied extensively in N-body Cold Dark Matter (CDM) simulations. Dark matter halos have been shown to exhibit a universal density profile, of which the most common parametrization is referred to as the NFW profile (Navarro et al. 1997). More recent studies have determined that dark matter profiles deviate on average slightly from this two parameter description, and are better described by the Einasto profile, which introduces one extra parameter that mitigates the tendency for the measured concentration to spuriously depend on the innermost radius in the fit to the density profile (Navarro et al. 2004; Merritt et al. 2005;

Gao et al. 2008). The regularity in dark matter halos is one of the most robust predictions of hierarchical structure formation.

Galaxies are believed to form inside dark matter halos via the cooling and condensation of baryons to their centers. Hydrodynamic simulations of hot gas in halos indicate that as this process occurs, baryonic physics affects the shape of the dark matter profile. As the baryons cool to the center, they begin to dominate the mass in the halo interior. The dark matter feels the change in the gravitational potential and is drawn into the center, steepening the central profile. The response of the dark matter to the cooling baryons has been modeled as the adiabatic contraction (AC) of a series of spherical shells under the assumptions of spherical symmetry, circular particle orbits, and conservation of angular momentum (Blumenthal et al. 1986). This treatment has been modified to account for the orbital eccentricity of particles in Gnedin et al. (2004), and has been shown to re-

* schulz@ias.edu

produce the profiles of halos in hydrodynamical simulations at the 10–20 per cent level.

Realistically, the AC process is synchronous with other more violent processes of merging and accretion. Older galaxies, in which the gas has been converted to stars long ago, continue to suffer dissipationless merging that has been argued to remove the influence of AC (Gao et al. 2004; Johansson et al. 2009). If a galaxy has had some portion of its baryonic content shock heated and removed to the warm-hot intergalactic medium where it is no longer seen, then potentially the contraction of the dark matter halo will be smaller, while the halo mass will remain the same. The hydrodynamic simulations of Rudd et al. (2008) suggest that the AC of the halo persists at a level that affects the matter power spectrum at halo-sized scales. On the other hand, Naab et al. (2007) suggest that the galaxy formation history, and specifically whether recent growth is due to star formation versus due to mergers and/or accretion, influences whether adiabatic contraction occurs or whether the dark matter halo in fact becomes less concentrated. Due to the many theoretical uncertainties, an observational handle on the mass distribution in both the inner and outer regions of the halo is crucial.

The most reliable way to probe the dark matter is through its gravitational effects. Weak gravitational lensing (for a review, see Bartelmann & Schneider 2001) of background galaxies by a foreground dark matter halo, or galaxy-galaxy lensing, is one robust way to constrain the halo density profile. This method has been used to constrain halo density profiles outside of the regions where the influence of baryons is significant, for stacked galaxy samples (due to the lower signal) and for stacked and individual clusters (e.g. Dahle et al. 2003; Mandelbaum et al. 2006, 2008a; Okabe et al. 2009; Riemer-Sørensen et al. 2009). However, the inner regions of the halo where AC is important are typically inaccessible to weak lensing except perhaps for very deep space-based observations (e.g., Gavazzi et al. 2007 measure the weak lensing signal down to $10 h^{-1}$ kpc). In this regime, the number of available background galaxies is small, confusion of light from the lens galaxy can make the measurement of background galaxy shapes unreliable, and the weak lensing approximation may fail entirely on small scales. Progress can be made by combining weak lensing with another probe such as strong lensing or kinematics (e.g., Kneib et al. 2003; Gavazzi et al. 2007; Limousin et al. 2007; Bradač et al. 2008; Corless et al. 2009; Oguri et al. 2009; Umetsu et al. 2009).

In this paper, we combine weak lensing observations in the halo, outside of the central regions ($> 70 h_{70}^{-1}$ kpc), with dynamical measurements that probe the central regions ($< 10 h_{70}^{-1}$ kpc) of a stacked sample of elliptical galaxies from the Sloan Digital Sky Survey (SDSS). This approach allows us to constrain the density profile over a large dynamic range of scales. An alternate approach is to combine strong and weak lensing measurements, as in Gavazzi et al. (2007); however, our approach allows the use of a statistical sample of elliptical galaxies, rather than being constrained only to those that are strong lenses. Finally, integral-field spectroscopy (e.g., de Zeeuw et al. 2002; Cappellari et al. 2006) can be used to probe the galaxy density velocity distribution and therefore infer the matter profile in detail within the effective radius, which in comparison with stellar population synthesis models applied to the light distribution,

can be used to infer the amount of dark matter within the effective radius. However, the connection to the profile on much larger scales is unclear, so it is impossible on the basis of IFU observations alone to distinguish between an adiabatically contracted halo versus a halo that is very massive overall.

In section 2, we describe the sample of galaxies used in the analysis. In section 3, we begin with the dynamical mass measurement and then combine it with weak lensing observations. We further divide the sample along the mean size-luminosity relation and show that the scatter from this relation correlates with properties of the underlying dark matter profile. We conclude in section 4. Throughout, we use comoving distances unless specifically noted, with lowercase r representing the three dimensional separation and uppercase R representing projected quantities. We have assumed a flat Λ CDM cosmology with $\Omega_m = 0.3$ and $\Omega_\Lambda = 0.7$. Since we must compare stellar masses, which scale like h^{-2} (for Hubble parameter $H_0 = 100h$ km/s/Mpc), with dynamical and halo masses, which scale like h^{-1} , our results are by necessity dependent on the choice of h . We use $h = 0.7$ for all quantities, and explicitly indicate their h -dependence using h_{70} ; e.g., halo masses are indicated with $h_{70}^{-1} M_\odot$, stellar masses with $h_{70}^{-2} M_\odot$, distances with h_{70}^{-1} kpc, ratios of stellar to dynamical mass with h_{70}^{-1} , and similarly for other quantities. When relating results from other works that use $h = 1$, we simply use h^{-1} kpc or $h^{-1} M_\odot$.

2 OBSERVATIONAL SAMPLE

The lens and source samples that we use are from the SDSS (York et al. 2000), which has imaged roughly π steradians of the sky, and followed up approximately one million of the detected objects spectroscopically (Eisenstein et al. 2001; Richards et al. 2002; Strauss et al. 2002). The imaging was carried out by drift-scanning the sky in photometric conditions (Hogg et al. 2001; Ivezić et al. 2004), in five bands (*ugriz*) (Fukugita et al. 1996; Smith et al. 2002) using a specially-designed wide-field camera (Gunn et al. 1998). All of the data were processed by completely automated pipelines that detect and measure photometric properties of objects, and astrometrically calibrate the data (Lupton et al. 2001; Pier et al. 2003; Tucker et al. 2006; Padmanabhan et al. 2008). The SDSS was completed with its seventh data release, DR7 (Stoughton et al. 2002; Abazajian et al. 2003, 2004, 2005; Finkbeiner et al. 2004; Adelman-McCarthy et al. 2006, 2007, 2008; Abazajian et al. 2009), from which we derive our sample, though it does not cover the entire area.

2.1 Lens sample

The lens galaxies are taken from the spectroscopic sample, for which we used the NYU Value Added Galaxy Catalog (VAGC, Blanton et al. 2005). For the portion of the analysis that requires stellar masses, we have used the stellar masses of Kauffmann et al. (2003) updated for DR7¹.

¹ www.mpa-garching.mpg.de/SDSS/DR7/Data/stellarmass.html

The lens population is selected from the SDSS spectroscopic sample using the following criteria. These criteria are designed to select elliptical or S0 type galaxies with little or no rotational support that are the central galaxy in their dark matter halos, so that SDSS velocity dispersion measurements can be reliably translated into dynamical masses, and the weak lensing signal more easily interpreted. All quantities are from the standard SDSS reductions (rerun 137), unless specifically mentioned.

- $0.02 < z < 0.35$: We select lenses from the Main spectroscopic sample with these spectroscopic redshifts.
- $g - r > 0.8$: This cut in rest-frame colour ensures that we are looking only at red galaxies with little to no active star formation. We have used model magnitudes k -corrected to redshift 0.1 from the VAGC (Blanton & Roweis 2007). The model magnitudes are extinction corrected using the reddening maps of Schlegel et al. (1998) and extinction-to-reddening ratios from Stoughton et al. (2002).
- $\sigma_v > 70$ km/sec: This cut ensures that the stellar velocity dispersion in the SDSS fiber can be reliably determined, given the resolution of the SDSS spectrograph.
- $R_{90}/R_{50} > 2.6$: This cut on the ratio of the Petrosian r -band 90 and 50 per cent light radii helps to ensure that we are selecting elliptical lens galaxies. The fact that the intensity profiles of ellipticals are more concentrated than those of spiral galaxies (Shimasaku et al. 2001) motivates this criterion.
- $b/a > 0.7$: We select objects with large values of the minor to major semi-axis ratio, obtained from model fits to a de Vaucouleurs profile. This cut will eliminate large edge-on spiral galaxies (which may pass our colour cuts due to internal reddening), as well as elliptical galaxies with substantial rotation velocities that tend to flatten them.
- Central: To ensure the lens galaxy is the central galaxy in its dark matter halo rather than a satellite galaxy, we assume that the brightest galaxy in a halo will be at the center. Thus we discard galaxies that have a brighter neighbor within a cylinder centered on the galaxy. Following Reid & Spergel (2009), we select a cylinder of diameter $1.6 h^{-1}$ Mpc (using $h = 1$ here for consistency with that work) and ± 864 km/s along the line of sight. Due to fiber collisions in the SDSS, some of the galaxies that pass the cuts imposed on the Main spectroscopic sample lack redshifts. These galaxies are not included in our lens catalog, but for the purposes of finding brighter neighbors, the redshift of the colliding galaxy is assigned to the object with no redshift to decide whether it falls into the cylinder.

In addition to the selection made on the basis of lens galaxy properties, we also removed galaxies that lacked source galaxies in the background, that lacked stellar mass estimates, and that fell outside the mask of the random catalogs available in the VAGC. These cuts eliminated approximately 15 per cent of the galaxies.

For the bulk of our analysis, we have divided the 75 086 lenses into three luminosity bins. The faintest bin contains half the lenses, the middle bin contains 1/3, and the brightest bin contains 1/6 of the sample to roughly balance the signal-to-noise ratio (S/N) in the weak lensing measurements. Figure 1 shows the redshift distribution for each of these bins, and Fig. 2 shows the distribution of stellar masses. For each galaxy, we use the median of the PDF of

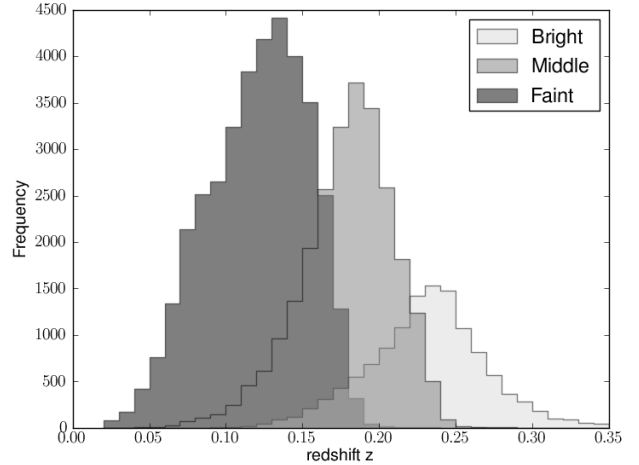


Figure 1. The redshift distribution of the the three luminosity bins used in this analysis.

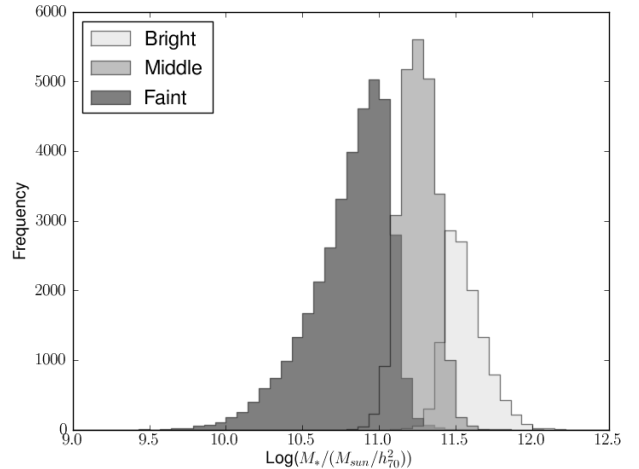


Figure 2. The distribution of stellar masses.

the stellar mass as our stellar mass estimate. A histogram of the comoving half light radii is plotted in Fig. 3

2.2 Source sample

The source galaxies (with shape estimates) are taken from the SDSS photometric catalogs, with additional processing and selection cuts described in Mandelbaum et al. (2005a). This source sample contains over 30 million galaxies from the SDSS imaging data with r -band model magnitude brighter than 21.8, with shape measurements obtained using the REGLens pipeline, including PSF correction done via re-Gaussianization (Hirata & Seljak 2003), and with cuts on apparent size relative to the PSF designed to avoid various shear calibration biases. The overall calibration uncertainty due to all systematics was originally estimated to be eight per cent (Mandelbaum et al. 2005a), though the redshift

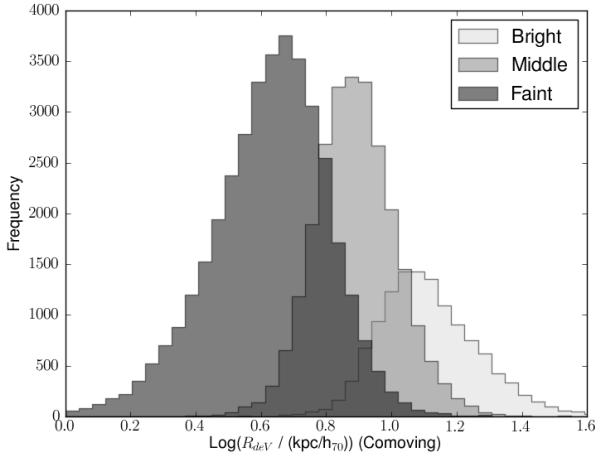


Figure 3. A histogram of the (comoving) projected half light radii for each of the three luminosity samples.

calibration component of this systematic error budget has recently been decreased due to the availability of more spectroscopic data (Mandelbaum et al. 2008b).

For the lensing analysis, a subsample of the total source catalog is used in probing the smaller radii, $R < 100h^{-1}$ kpc (described in section 3.2). This procedure is a result of the analysis in Mandelbaum et al. (2006), which found that for bright elliptical lenses, use of the full source sample led to inclusion of satellites of those lenses that were intrinsically aligned towards their hosts, thus contaminating the lensing measurement. The LRG sources used at small separations were identified using colour cuts described in Mandelbaum et al. (2005a) to have very little contamination from galaxies below $z = 0.4$, thus minimizing contamination from intrinsic alignments with our lenses, which are well below this redshift.

3 RESULTS

Table 1 summarizes all the properties of the lens sample used in this work. We now describe how we arrived at these numbers.

3.1 Dynamical mass measurements

We measure the dynamical mass at the 2D de Vaucouleurs scale radius for comparison with the weak lensing dark matter profile measurement, described later in section 3.2. The dynamical mass is inferred by assuming a relation between the velocity dispersion of stars inside the portion of the galaxy covered by the SDSS fiber (3 arcsec in diameter), and the mass enclosed within the 2D de Vaucouleurs scale radius. The mass is related to the velocity of particles on circular orbits as

$$v_c^2(r_{\text{phys}}) = \frac{GM(r_{\text{phys}})}{r_{\text{phys}}}, \quad (1)$$

but relating the circular velocity to the radial velocity dispersion σ measured in SDSS requires a model for the stellar

and dark matter mass distributions. The method for relating the two via the Jeans equation can be found in Padmanabhan et al. (2004). We have assumed the stars follow a Hernquist profile (Hernquist 1990) and the dark matter profile is an adiabatically contracted NFW profile, using the model of Gnedin et al. (2004). Since the sample is comprised of early type elliptical galaxies, we also assume that star formation has used all the available gas (Read & Trentham 2005, Morganti et al. 2006, Fukugita et al. 1998) and we neglect any contribution to the mass from gas in the central region. We assume that there is no radial anisotropy β in the Jeans equation defined as

$$\beta = 1 - \frac{\bar{v}_t^2}{\bar{v}_r^2} = 0 \quad (2)$$

where \bar{v}_r^2 is the radial velocity dispersion and \bar{v}_t^2 is the tangential velocity dispersion, which is not observable. Our results are insensitive to this assumption, as discussed section 3.4.

Fig. 3 compares the theoretical expectations for the velocity dispersion and circular velocity profiles for our middle luminosity bin. The velocity dispersion profile changes by < 4 per cent from $r/R_{\text{deV}} = 0.5$ to 2.5, allowing us to extrapolate the velocity dispersion measurements from the fiber radius to the half-light radius. Furthermore, we find that the circular velocity is proportional to the velocity dispersion at the 5 per cent level, allowing us to robustly convert velocity dispersions into dynamical masses. At the projected half light radius, we find $v_c = 1.7\sigma$. Thus we can invert Eq. 1 to solve for the dynamical mass.

$$M_{\text{dy}} = \frac{(1.7\sigma)^2 R_{\text{deV}}}{G(1+z)} \quad (3)$$

Here we explicitly divide by $1+z$ since our notation has R_{deV} in comoving coordinates. Fig. 2 of Padmanabhan et al. (2004) shows that these curves are extremely insensitive to the value of the radial anisotropy parameter β , even if β is not held constant with radius. The constant of proportionality is also insensitive (at ~ 5 per cent) to the stellar and DM mass profiles, and the details of the AC prescription, including no AC (Padmanabhan et al. 2004). Variations in these model quantities cause M_{dy} to shift at the level of ~ 10 per cent. We adopt this as the systematic uncertainty on the measurement of the total dynamical mass inside the SDSS fiber.

Notice that the velocity dispersion σ measured in SDSS is not measured at the projected half light radius R_{deV} , but rather at the radius subtended by the SDSS fiber. We appeal to the flatness of $\sigma(r)$ demonstrated in Fig. 4 and assume that this measurement will equal the velocity dispersion at the half light radius. The angular diameter subtended by the SDSS fiber at the redshift of the middle luminosity bin is marked with a vertical line on the plot.

We emphasize one detail: although the radius in Eq. 3 is the 2D projected half light radius, which is measured in SDSS by fitting to a de Vaucouleurs profile, the dynamical mass in Eq. 3 is an estimate of the 3D mass interior to that distance, not the mass in a 2D cylindrical projection through the halo out to that radius. Eq. 3 implies that at these radii the 3D dynamical mass is simply proportional to the radius (i.e., the profile is effectively isothermal), and we are choosing to make the measurement at the half-light

Luminosity	Sample	z	$M_*^{\text{Tot}}(\text{e10})$ $h_{70}^{-2} M_\odot$	$M(\text{e13})$ $h_{70}^{-1} M_\odot$	c	R_{deV} $h_{70}^{-1} \text{ kpc}$	$M_{\text{dy}}^{\text{Tot}}(\text{e10})$ $h_{70}^{-1} M_\odot$	$M_{\text{dy}}^{\text{DM}}(\text{e10})$ $h_{70}^{-1} M_\odot$	$M_{\text{nfw}}(\text{e10})$ $h_{70}^{-1} M_\odot$	f_* h_{70}^{-1}
$M_r < -21.27$	Full	0.22	36 ± 6	$5.7^{+0.9}_{-0.8}$	$8^{+1.6}_{-1.4}$	13.4 ± 0.5	49 ± 5	34 ± 6	19^{+4}_{-3}	0.31
$-21.27 < M_r < -20.54$	Full	0.17	18 ± 4	$2.4^{+0.4}_{-0.3}$	$7^{+1.4}_{-1.0}$	8.0 ± 0.4	21 ± 2	14 ± 2	$4.0^{+0.9}_{-0.6}$	0.35
$M_r > -20.54$	Full	0.11	7 ± 2	$0.7^{+0.2}_{-0.1}$	$9^{+4.0}_{-2.2}$	4.3 ± 0.3	7.3 ± 0.7	4.5 ± 1.0	$1.1^{+0.6}_{-0.3}$	0.38
$M_r < -21.27$	S/B	0.22	33 ± 5	$3.0^{+0.9}_{-0.8}$	8^{+3}_{-2}	10.0 ± 0.4	39 ± 3	25 ± 4	8^{+4}_{-2}	0.36
$M_r < -21.27$	L/D	0.22	38 ± 6	$6.2^{+1.3}_{-1.1}$	9^{+2}_{-2}	16.1 ± 0.6	57 ± 6	41 ± 7	30^{+7}_{-6}	0.28
$-21.27 < M_r < -20.54$	S/B	0.17	18 ± 5	$1.9^{+0.5}_{-0.4}$	6^{+2}_{-2}	6.5 ± 0.3	19 ± 1	11 ± 2	$2.2^{+0.9}_{-0.6}$	0.39
$-21.27 < M_r < -20.54$	L/D	0.17	18 ± 3	$2.8^{+0.8}_{-0.6}$	6^{+2}_{-2}	9.8 ± 0.4	24 ± 2	17 ± 2	$5.6^{+1.8}_{-1.4}$	0.32
$M_r > -20.54$	S/B	0.12	7 ± 2	$0.6^{+0.3}_{-0.2}$	8^{+7}_{-4}	3.5 ± 0.2	6.7 ± 0.6	3.9 ± 0.9	$0.6^{+0.6}_{-0.2}$	0.42
$M_r > -20.54$	L/D	0.11	7 ± 2	$0.6^{+0.3}_{-0.2}$	13^{+12}_{-5}	5.2 ± 0.3	7.9 ± 0.8	5.2 ± 1.0	$2.2^{+2.8}_{-1.0}$	0.35

Table 1. Properties of the three lens samples studied in this work. The upper part of the table shows the result for the full sample, and the lower part shows the division of the sample along the mean size-luminosity relation (Smaller/Brighter or Larger/Dimmer than the mean relation). The notation e10 is shorthand for ($\times 10^{10}$). Luminosities are in absolute r -band magnitude, galactic extinction- and k -corrected as described in section 2. The quantities M and c are fit to the weak lensing observations. The quantities z , M_* , R_{deV} (comoving coordinates) and DM M_{dy} are lensing weighted averages over the lenses in the sample, and the Total M_{dy} is obtained by adding $0.42M_*$ to the DM M_{dy} . M_{nfw} is the mass expected from an NFW profile with mass M and concentration c . The dynamical masses and M_{nfw} are measured inside R_{deV} . The value $h = 0.7$ has been inserted into the distance modulus. The fraction of mass contributed by the stars at R_{deV} is given by f_* , and depends on the value of h . Errors on M , c , and M_{nfw} are the 68 per cent CL obtained from bootstrap resampling of the NFW fits. Errors on M_*^{Tot} and R_{deV} are measurement errors. Errors on the dynamical masses come from a 10 per cent estimate of systematic error in the mapping between the velocity dispersion and the mass interior to R_{deV} .

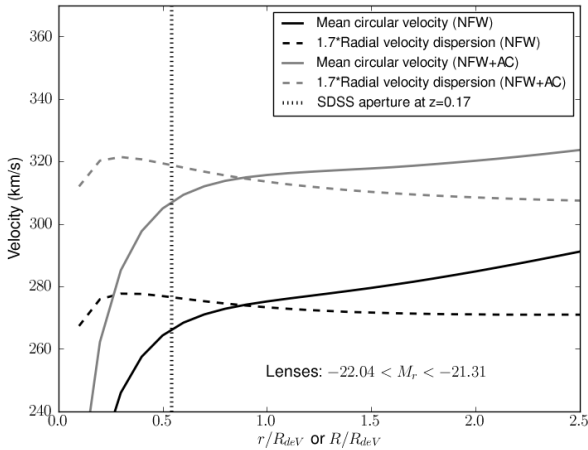


Figure 4. The circular velocity profile and radial velocity dispersion multiplied by 1.7, which causes the two to agree near the scale radius. The parameters used to generate these curves are taken from the intermediate lens sample. Note that these are relatively flat functions over a wide range of radii. The vertical line marks the angular size of the SDSS fiber at the mean redshift of the middle luminosity sample.

radius in order to be able to estimate the stellar contribution to the dynamical mass. The 3D stellar mass contained within the 2D projected half light radius R_{deV} can be derived from the Hernquist profile to be roughly 42 per cent of the total stellar mass. We subtract this from the total dynamical mass to derive the dark matter contribution to

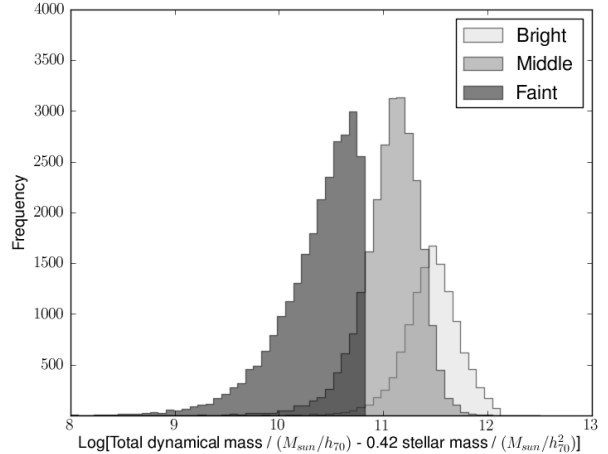


Figure 5. A histogram of the dark matter contribution to the dynamical mass for each of the three luminosity samples.

the dynamical mass at the half light radius. A histogram of this quantity is plotted in Fig 5.

3.2 Combining with weak lensing measurements

Weak gravitational lensing probes the differential surface density of the dark matter associated with the lens galaxies. On scales probed here, this surface density can be attributed to the dark matter halo; on larger scales, due to large-scale structure. Thus, on the scales less than $\sim 1 h_{70}^{-1} \text{ Mpc}$, we can

define the projected surface density via

$$\Sigma(R) = \int \rho(R, z) dz. \quad (4)$$

Here $\rho(r = \sqrt{R^2 + z^2})$ is the 3D density profile of the lens galaxies.

Weak lensing is sensitive to the differential surface density, defined as

$$\Delta\Sigma(R) = \bar{\Sigma}(< R) - \Sigma(R) = \gamma_t(R)\Sigma_c, \quad (5)$$

where the critical surface density Σ_c is

$$\Sigma_c = \frac{c^2}{4\pi G} \frac{D_S}{D_L D_{LS}(1 + z_L)^2} \quad (6)$$

in comoving coordinates. Here, D_L and D_S are the angular diameter distances to the lens and source galaxies, and D_{LS} is the angular diameter distance between the lens and source galaxies. The right side of Eq. 5 shows how $\Delta\Sigma(R)$ is related to the observable γ_t , the mean tangential shear of source galaxies behind the lens galaxies. This equation is true in the weak lensing limit ($\gamma_t \ll 1$) in the presence of an axisymmetric mass distribution, which is achieved by our measurement procedure.

The measurement is performed by stacking lens galaxies based on their luminosities. The stacking procedure allows us to achieve sufficient source number density to measure the shear signal, and therefore $\Delta\Sigma$, of the composite object. To do so, we measure the tangential shear of all source galaxies in annular bins around the lens positions. The details of the signal computation are described in appendix A. We are implicitly assuming that on the scales used for our measurement, the shearing of background galaxies is caused only by the lens halos, and not by other nearby halos or infalling dark matter (in the language of the halo model, we neglect the two-halo term). For the few lenses that may be satellites despite our selection criteria designed to avoid them, we also neglect the contribution from the host halo. Furthermore, we neglect the radial window that enters the line-of-sight projection in Eq. 4, given that the window is far broader than the characteristic scale of our lenses.

To generate model lensing signals that can be compared against the measurements, we fit the two-parameter NFW profile to the lensing data. The spherical NFW density profile is defined as

$$\rho_{\text{NFW}}(r) = \frac{\rho_s}{(r/r_s)(1 + r/r_s)^2}. \quad (7)$$

We can express it in terms of two parameters, the mass M within which the average density is equal to some overdensity (here, 200 times overdense compared to the mean background density $\bar{\rho}$), and the concentration, which is the ratio of the virial radius to the scale radius $c = r_{\text{vir}}/r_s$. M and c can be related to ρ_s and r_s via

$$M = \frac{4\pi}{3} r_{\text{vir}}^3 (200\bar{\rho}) = 4\pi \int_0^{r_{\text{vir}}} \rho(r) r^2 dr \quad (8)$$

$$\bar{\rho} = \Omega_m \rho_c = \Omega_m \frac{3H^2}{8\pi G}. \quad (9)$$

Here Ω_m is the matter energy density today relative to the critical density, and H is the Hubble parameter. Our model signal can then be generated for a given value of M and c by projecting the profile along the line of sight (Eq. 4) and integrating to obtain $\Delta\Sigma$ (Eq. 5).

Our use of a spherical NFW profile is justified because of the large number of lenses stacked, as verified by Mandelbaum et al. (2005b). We use the NFW density profile rather than the Einasto profile,

$$\rho_{\text{Einasto}}(r) = \rho_s e^{(-2/\alpha)[(r/r_s)^\alpha - 1]}, \quad (10)$$

but note that the two profiles are quite similar on weak lensing scales, though they are substantially different at smaller scales. One consequence of this choice is that the estimate of the concentration may potentially be systematically biased in a way that depends on the innermost radius used in the fit. The impact of a systematic offset in concentration is discussed in section 3.4. However, as shown in Mandelbaum et al. (2008a), fitting the galaxy cluster weak lensing profile on these scales for a concentration gave the same result to within several per cent when using an NFW profile and an Einasto profile.

The fitting procedure involves two steps. In the first step, for each luminosity bin we fit the profile to the observed $\Delta\Sigma$ using the non-linear least-squares algorithm of Levenberg-Marquardt. Here, we use all data from $70 < R < 2000 h_{70}^{-1} \text{ kpc}$ even though this may include scales on which lensing from large-scale structure is important. Our choice of minimum radius was motivated by the fact that ellipticity measurements of source galaxies closer than $R < 70 h_{70}^{-1} \text{ kpc}$ to the lens center may be unreliable due to confusion of light from the lens, and smaller source counts. The resulting profile with (M, c) for each luminosity bin is used to estimate a virial radius for each bin. We then fit again, truncating the data at that virial radius to avoid significant contributions to $\Delta\Sigma$ from material outside the lens halo (two-halo term). This procedure results in fitting fewer radial bins for the faintest sample. The brightest and intermediate bins are fit in the interval $70 < R < 850$ and the faintest bin in the interval $70 < R < 570 h_{70}^{-1} \text{ kpc}$.

The lensing result and the NFW fit are shown in the top panel of Fig. 6. The heavy solid line shows $\Delta\Sigma$ for the best fit NFW model, while the thin solid line shows the extrapolation of the NFW result to small radii. The points show the lensing measurements. The dashed lines show a 68 per cent confidence level estimate for the error on the NFW result for the middle sample. The errors are derived by bootstrap resampling 200 regions on the sky 1000 times, and recomputing the fit for each resampled dataset. The curves show the 16th and 84th percentile values of $\Delta\Sigma(R)$ determined by rank-ordering the fits to the bootstrapped datasets.

The bottom panel of Fig. 6 shows the (3D) integrated mass interior to the comoving radius r the NFW model of the middle sample shown in the top panel. For comparison, we also plot the enclosed mass for the Einasto profile, using the same mass and concentration parameters, and fixing the shape parameter following Gao et al. (2008). The horizontal scales in the two panels are the same. The total dynamical mass (upper point) and the dark matter contribution to the dynamical mass (lower point) are plotted at the position of the 2D de Vaucouleurs half light radius of the lens galaxies. The half light radius and dynamical masses shown are the lensing weighted mean value for the lenses in this luminosity bin. The lensing weights, which can be found in appendix A, are assigned to each lens-source pair, and include redshift information and error on the shape measurement of

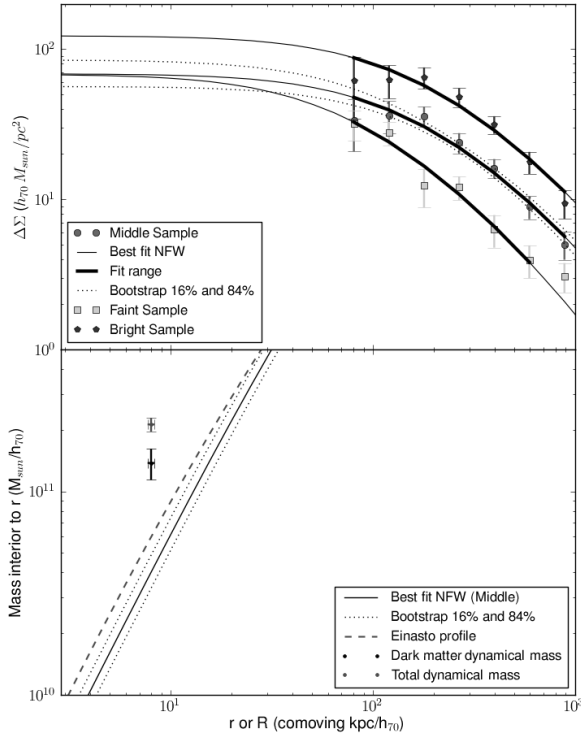


Figure 6. Top: Points are the weak lensing measurement. Solid lines show the differential surface density for the best fit NFW model. Dotted lines show 16 and 84 per cent contours from fits to bootstrap resampled datasets. **Bottom:** Solid lines show the integrated mass interior to r , and dotted lines show a bootstrap estimate for error in NFW. The dashed curve shows the result for an Einasto profile for comparison. The upper point shows the total dynamical mass, while the lower point shows the dark matter contribution to the dynamical mass after subtracting the estimated contribution from stellar mass.

the source. To deduce the dark matter contribution to the dynamical mass, we subtract 42 per cent of the total stellar mass (the fraction of stars enclosed within a 3D radius corresponding to the 2D half light radius) from the total dynamical mass. The error bar on R_{deV} comes from the measurement error. The error bar on the total dynamical mass is estimated to be ~ 10 per cent, from variations in the input modeling from Eqn. 3 and from differences between R_{deV} and the portion of the galaxy covered by the SDSS fiber. The error bar on the dark matter dynamical mass comes from combining this systematic error in the total dynamical mass with measurement errors in the stellar masses.

Although the NFW curve has been extrapolated inward by more than an order of magnitude in transverse separation, it is noteworthy that the total dynamical mass in the interior of the galaxy exceeds the NFW prediction by eleven standard deviations. Even when the contribution of stars has been accounted for, there appears to be over a factor of two more dark matter mass in the central region of the

galaxy (four standard deviations) than what is seen in halos from N-body simulations of large scale structure.

This result is consistent with earlier attempts to observe the density profile of elliptical galaxies. Jiang & Kochanek (2007) used stellar dynamical and strong lensing measurements of 22 early-type galaxies from the Sloan Lens ACS Survey (SLACS) to constrain the total matter profile near the effective radius. These data alone are not enough to distinguish between a model with and a model without adiabatic contraction; however, when they include weak lensing constraints on $100h^{-1}$ kpc scales from Gavazzi et al. (2007), they find that the models with adiabatic contraction are strongly favored. For their analysis, they used the Blumenthal et al. (1986) model for adiabatic contraction, which predicts a more significant effect than the Gnedin et al. (2004) model used in our work.

3.3 Comparison with adiabatic contraction model

It is well known that baryonic physics is expected to affect the form of the dark matter profile in galaxy halos, so it is not entirely surprising that the profile departs from N-body predictions in a region where the mass is largely made up of stars. Exactly how the baryons affect the dark matter distribution, and whether their effect is transient or enduring is however a matter of some theoretical debate. On the one hand, the dark matter is expected to fall into the cuspy deep gravitational potentials that are created when baryons cool and condense to form galaxies, a process known as adiabatic contraction (AC) that further deepens the central potential. In the simulations of Rudd et al. (2008), these steeper potentials are seen to persist, and the impact of the baryons is evident on the matter power spectrum, principally through the change in the dark matter profiles inside the virial radii of halos, particularly around cluster masses of $10^{14}h^{-1}M_{\odot}$. On the other hand, there is some debate as to whether spiky central cusps will survive the onslaught of subsequent major and minor merger activity expected in hierarchical models of structure formation. In the simulations of Johansson et al. (2009), adiabatic contraction is seen initially, but is transformed to a cored central potential through gravitational heating from mergers. To date, there have been very few observational studies that can probe the dark matter halo over the large range of scales required to test the AC hypothesis. We make an attempt here by comparing the AC model of Gnedin et al. (2004) to the dynamical mass data, shown in Fig. 7.

Each of the panels in Fig. 7 is analogous to the bottom panel of Fig. 6, but each quantity is now divided by the best fit NFW relation (solid curve in Fig. 6) so as to present the results on a linear scale. Note that the best fit NFW is different for each panel. The 3d stellar fractions of the total mass at the half light radius are $f_{\star} = 31, 35$ and $38h_70^{-1}$ per cent (from bright to faint). The curves in Fig. 7 show the AC models of Gnedin et al. (2004) (dashed) and Blumenthal et al. (1986) (dot-dashed). These are computed using the publicly available CONTRA code (Gnedin et al. 2004). To model AC, we use the mass and concentration from the weak lensing measurements, and make a few reasonable assumptions. We assume that for these elliptical lens galaxies all of the gas has been converted into stars (Read & Trentham 2005, Morganti et al. 2006, Fukugita et al. 1998), so that

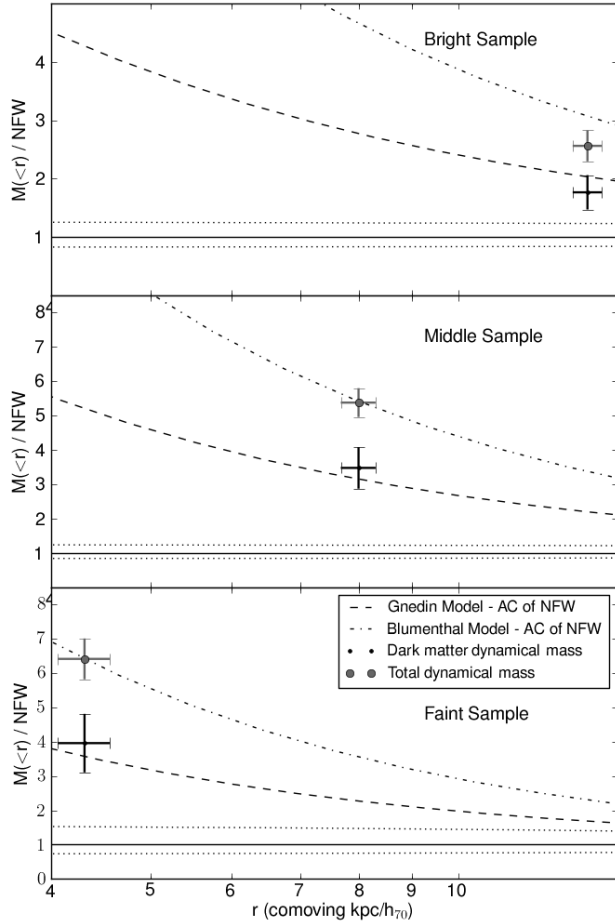


Figure 7. All curves and points are defined in the same convention as in the bottom panel of Fig. 6, with the addition of a dashed line showing the predictions including AC. The non-AC NFW model has been divided out (solid line at 1) so as to present the results on a linear scale. The (top, middle, bottom) panel shows the (brightest, intermediate, faintest) lens sample.

the baryon fraction is given by the stellar mass divided by the best-fitting dark matter halo mass. This assumption is robust for the fainter bins but may begin to break down for the brightest bin, for which the mass approaches the group scale. We also assume the baryons ultimately arrange themselves into a Sérsic profile with $n = 4$, i.e. a de Vaucouleurs profile, with scale radius R_{dev} converted as in the appendix of Padmanabhan et al. (2004).

It is remarkable that in all three luminosity bins, the model NFW profile with adiabatic contraction agrees with the inferred contribution of dark matter to the total dynamical mass. This AC model leads to enhancements of the dark matter contribution to the dynamical mass that are approximately factors of 4, 3.5, and 2 for the faint, middle, and bright samples respectively. The disagreement of the data with the extrapolated pure NFW profile (i.e., without AC) is significant at the 3.5σ , 4σ , and 2.5σ level, respectively. The apparent agreement between the total dynamical mass and the Blumenthal et al. (1986) model of AC is a coinci-

dence; for this to be meaningful, none of the mass could be in stars.

3.4 Potential systematic errors

In this section, we discuss a number of systematic uncertainties present in this measurement that make the very close agreement between the AC model and the measurement mildly surprising.

3.4.1 Initial mass function

The most significant concern for potential systematic error lies in the determination of the stellar mass. The stellar masses are computed assuming a Kroupa Initial Mass Function (IMF, Kroupa 2001), which is calibrated by measuring the mass function of stars in the solar neighborhood. While it is expected that some level of churning will bring stars from orbits in all parts of the galaxy close to the solar neighborhood, the degree of churning is very uncertain. More importantly, galaxies of different ages and types have different metallicities, and the shape of the IMF may well depend on metallicity. In Kauffmann et al. (2003), the sensitivity of the stellar masses to the choice of IMF was investigated, and it was shown that assuming a Salpeter (Salpeter 1955) IMF with a lower mass cutoff at $0.1M_{\odot}$ systematically increased the stellar masses by approximately a factor of 2. However, the amount of increase in the stellar masses will quantitatively depend on how the low mass end of the (divergent) Salpeter IMF is regularized. It is interesting to contemplate that aside from the question of AC, this measurement of the dynamical mass can be thought of as a constraint on the IMF, in the sense that the stellar mass cannot exceed the total dynamical mass.

To fully explain the observed dynamical masses with no adiabatic contraction of the dark matter, the stellar masses would have to increase by a factor of 1.9, 2.3 and 2.2 for the bright, middle and faint samples. However, Cappellari et al. (2006) present a challenge to this alternative explanation. They use detailed integral field spectroscopy observations to infer dynamical masses within the effective radius for 25 nearby E/S0 galaxies, and compare them with the predicted stellar masses from stellar synthesis models. They find that for some of the galaxies, the predicted stellar masses with a Salpeter IMF exceed the dynamical masses, which suggests that if we require the same IMF for each galaxy, then the Salpeter IMF is too bottom-heavy. In contrast, the Kroupa IMF gives stellar masses that are 30 per cent lower than with the Salpeter IMF (for their choice of cutoff mass), causing all the stellar masses to be less than or equal to the inferred dynamical masses. Thus, the conclusion that the IMF is very bottom-heavy (instead of accepting the AC hypothesis) may be difficult to reconcile with these IFU observations of elliptical and S0 galaxies.

3.4.2 Other stellar mass uncertainties

There are other systematic effects in the stellar mass estimates that are expected to be subdominant to the IMF uncertainties. For example, the effects of aperture bias (the fact that the M_*/L are derived from the region of the galaxy

covered by the fiber, not the whole galaxy) are estimated to be smaller than that of IMF uncertainties. Also, aperture bias is more problematic for galaxies with both differently-coloured bulge and disk contributions than for the pure ellipticals of which our sample is composed. See Kauffmann et al. (2003) for a more full discussion of all stellar mass-related systematics.

3.4.3 Initial conditions

Another systematic uncertainty relates to the conditions under which adiabatic contraction initially occurred. The process of AC happens while the baryonic component is still in gaseous form, whereas the measurement is being made on galaxies that have converted nearly all of the gas into stars. Presumably several (major or minor) mergers have occurred in the interim, whose qualitative effect will be to raise the mass and lower the concentration of the halo. If the baryon fraction of the merging objects differs from that of the parent halo, the baryon fraction will also have evolved since the time AC was occurring. To quantify how sensitive the AC result is to changes in the input parameters, we show in Fig. 8 the effects of a 30 per cent variation in halo mass, concentration, scale radius of the baryon component, and baryon fraction.

The CONTRA code accepts the baryon mass fraction as an input, and returns the pre-contracted and post-contracted curves in units where the mass has been scaled to the NFW virial mass, which we measure in the lensing analysis. We define the baryon fraction as $f_b = M_*/M$ (assuming that all the gas has been converted to stars)². The top two panels of Fig. 8 show the result of varying the halo mass M , in one case fixing the baryon fraction (top) and in the other case allowing the variation of M to affect the baryon fraction (second panel). In the top panel, changing the mass simply scales the curves up and down. The second panel shows that the change from scaling the mass in the top panel is nearly exactly offset at these radii by the effect of decreasing the baryon fraction. This result can be understood by comparing the top panel with the bottom panel (where only the stellar mass is scaled). A decrease in stellar mass implies a decrease in the baryon fraction, and since the deviation from the fiducial model is roughly the same size in the top and bottom panels, the effects cancel one another out in the second panel. One other noteworthy feature in Fig. 8 is that the effect of increasing the baryon scale radius changes the level of AC in the opposite sense than the other 4 curves. We conclude that there is a modest sensitivity in the model to these quantities that could change the prediction at a level comparable to the measurement error of the dynamical mass (indeed this is the reason we selected a 30 per cent variation). This sensitivity is not so large as to invalidate the result for reasonable (tens of per cent) shifts in these parameters.

² Please note this is distinct from f_* in Table 1, which indicates the fraction of the total dynamical mass that is in stars within a sphere of radius equal to the half light radius R_{deV} .

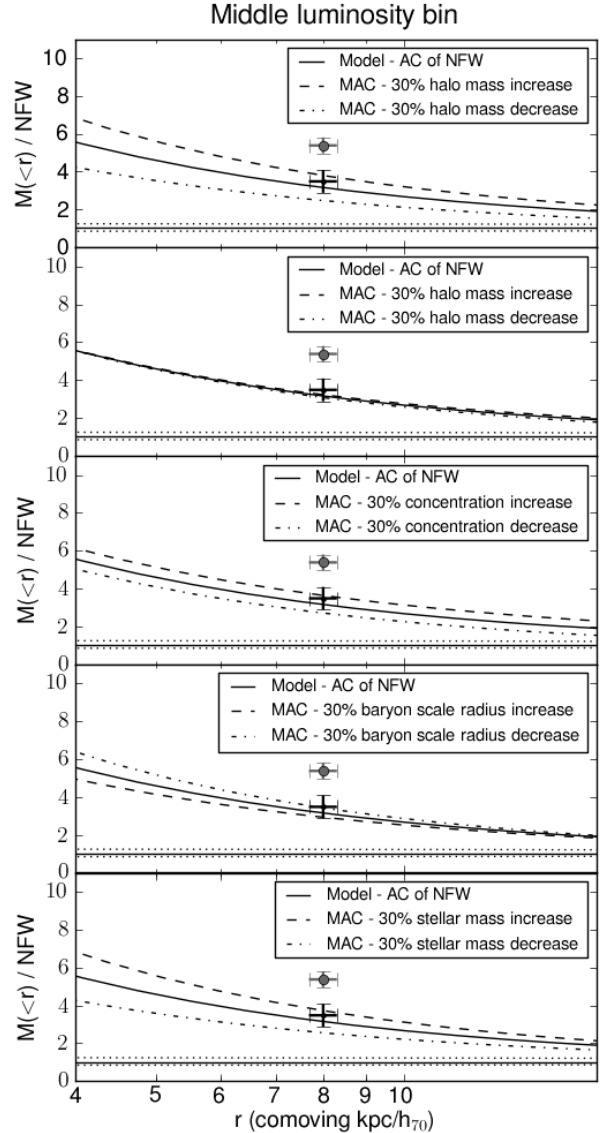


Figure 8. Each panel shows AC of the best fit NFW model (Solid curve), the total dynamical mass (upper grey point) and the dark matter contribution to the dynamical mass (lower black point). The dashed [dot-dashed] curve shows the impact on AC of increasing [decreasing] the halo mass (upper), concentration (upper middle), scale radius of the baryons (lower middle), and stellar mass (lower). All results have been divided by the non-AC best fit NFW model.

3.4.4 Dynamical mass assumptions

It is quite probable that the lens sample violates the assumption that the radial anisotropy parameter β is zero. It has already been shown in Padmanabhan et al. (2004) that the measured velocity dispersion is insensitive to the value of the radial anisotropy parameter. However it is also worth noting that for this type of galaxy, the anisotropy is much more likely to be radial rather than tangential (Cappellari et al. 2007). The impact of assuming no radial anisotropy for such objects will be to systematically underestimate the dynamical mass within the half light radius. A similar systematic ef-

fect that causes the dynamical mass to be underestimated is if the galaxies have some moderate rotational support. Both of these effects strengthen the conclusion that there appears to be more mass than predicted by simple extrapolation of the NFW profile; our dynamical mass measurements can be considered a lower bound.

3.4.5 Spread in the properties of the lens subsamples

Finally, our analysis uses relatively broad luminosity bins (because of the need for large lens samples to measure the lensing signal at reasonable S/N). Unfortunately, this means that a large amount of averaging takes place, which could muddy the interpretation of the results. We have attempted to ameliorate this effect by computing lensing-weighted average quantities (stellar masses, dynamical masses, half-light radii, and so on) to compare against the best-fitting dark matter halo mass. This procedure should help make the different kinds of measurements more comparable. However, Mandelbaum et al. (2005b) show that for lens samples with halo mass distributions that are more than a factor of five wide, the best-fitting halo masses lie somewhere above the median and below the mean, an effect that can be as large as several tens of per cent in extreme cases. Since Fig. 8 shows that changing the halo mass and other properties by 30 per cent does not change the AC predictions by more than about 1σ , we anticipate that our neglect of the bin width (which is unknown, in the case of the halo mass) will not substantially alter our conclusion that the AC model is consistent with our findings.

3.5 Splitting along the size-luminosity relation

It is interesting to ask if the level of excess mass in the galaxy interior correlates with other galaxy properties. There is evidence that a galaxy's environment and merger history directly impact the concentration and relative distributions of baryons and dark matter (Abadi et al. 2009 and references therein). It has also been suggested that multiple major or minor mergers may erase some of the effects of adiabatic contraction (Johansson et al. 2009). Since elliptical galaxies lie tightly on a fundamental plane, it would also be interesting if small departures correlate strongly with the form of the galaxy's dark matter profile. Fortunately, there is enough signal in the data to support one further level of subdivision in the analysis. We have opted to examine these questions by dividing each luminosity bin along the mean size-luminosity relation, which is a projection of the fundamental plane. The mean relation in our sample is

$$\log(R_{\text{deV}}) = 0.722 + 0.598 * ((-20.44 - M_r)/2.5) \quad (11)$$

where R_{deV} is in units of h_{70}^{-1} kpc. The results are presented in Table 1 and Fig. 9. The upper set of curves (dashed lines) show the departure from NFW (solid line at 1) due to AC for the smaller/brighter sample. The lower set of curves (dot-dashed lines) show AC for the larger/dimmer sample. The points on the left (right) correspond to the smaller/brighter (larger/dimmer) sample. Table 1 indicates that for the faint sample, we are unable to simultaneously constrain M and c for these subsamples divided along the mean size-luminosity relation. Therefore, in the bottom panel of Fig. 9, we adopt

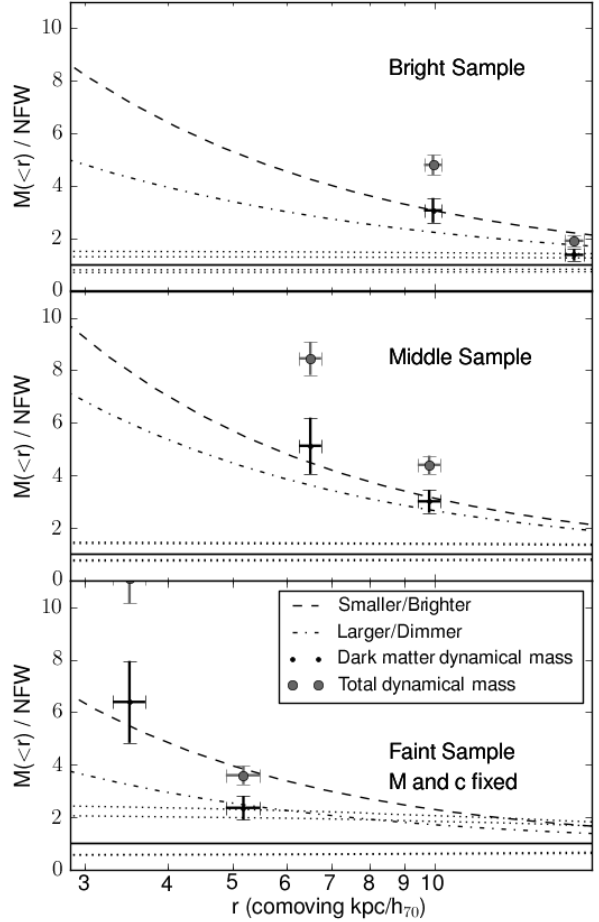


Figure 9. Three luminosity bins are shown from brightest (top) to dimmest (bottom panel). In each panel, curves on the top (bottom) show the AC results for lens subsamples that are smaller and brighter (larger and dimmer) the mean size luminosity relation. The solid lines with dotted error estimates show the enclosed mass for the NFW model that best fits the weak lensing data. The total observed dynamical mass (upper grey point) and the dark matter contribution to the dynamical mass (lower black point) plotted at the position of the half light radius. Points on the left (right) are the smaller/brighter (larger/dimmer) sample. Because the mass and concentration cannot be independently constrained for the two subsets of the faintest sample, M and c are fixed to the values of the composite faint sample (top level of Table 1).

the M and c from the composite sample (row 3 of Table 1). As a result, for the top two panels, the AC curves and data points for the two subsamples have been divided out by a different non-contracted NFW model; on the bottom panel, by the same model.

Table 1 shows that the halo masses and half-light radii of the smaller/brighter (S/B) sample are smaller than those of the larger/dimmer (L/D) sample, but the stellar masses and concentrations of the two populations are nearly the same. Fig. 9 indicates that the total dynamical mass at the half light radius is much more enhanced above the NFW prediction for the S/B sample than for the L/D sample.

There are competing effects driving this trend; it is helpful to refer to Fig. 8 in deciphering the result. Since the stellar masses are equivalent, the smaller halo masses for the S/B sample imply a larger baryon fraction f_b than in the L/D sample. Just as in panel two of Fig. 8, the increase in mass is offset by the decrease in the baryon fraction in comparing the S/B to the L/D sample. The concentrations of the two samples do not change very much, but the significant change in the baryon scale radius R_{dev} drives the overall trend. Since the S/B sample has a larger baryon fraction, and more of the baryons are concentrated toward the center of the halo, the effects of AC are more pronounced than in the L/D sample, even though the L/D sample has higher overall halo mass. There is also a higher stellar mass fraction $f_* = (0.42M_*)/M_{\text{dy}}^{\text{Tot}}$ at the half light radius for the S/B sample than for the L/D, although part of this effect could be accounted for by non-homologous profiles (P. v. Dokkum, priv comm).

An alternate interpretation of this result might be that the stellar IMF for the S/B sample has more mass in small faint stars than the IMF for the L/D sample (see the discussion of systematic error in Section 3.2 above), or potentially some combination of these two effects. The IMF interpretation requires us to discard the idea of a universal IMF for all elliptical galaxies.

Since it is likely that the S/B sample had its stellar population in place at earlier times, and that the L/D has potentially experienced merger activity more often or more recently, it would be very interesting in the future to correlate the level of AC with other indicators of age or merger activity. It is also interesting to note that the L/D subsamples within each luminosity bin have consistently larger halo masses than the S/B subsamples, despite the fact that their stellar masses are very similar. This result suggests that different star formation histories (that led to the different appearance of the stellar components at fixed stellar mass) also correlate with different accretion histories for the dark matter halos.

3.6 Comparison with previous work

Here we discuss how our results compare with previous, related observations. We first compare with Padmanabhan et al. (2004), which is relevant due to the similar sample definition and methodology. Since that work did not have any observational method of constraining the profile on large scales, we simply compare against their determination of the 3d stellar mass fraction f_* within the half-light radius. The relevant comparison is against figure 8 of that paper, which shows M_{dy}/M_* (i.e., our f_*^{-1}) as a function of the galaxy apparent size, for galaxy subsamples split by stellar mass. For our three relatively broad luminosity subsamples, we have typical values of half-light radius range from 4 to $13h_{70}^{-1}\text{kpc}$ and typical $1/f_*$ ranging from 2.6 to $3.2h_{70}$; Padmanabhan et al. (2004) find values of $1/f_*$ that range from 2–4 (depending on the stellar mass, in narrower bins than ours), which is consistent with our findings.

The comparison with Gavazzi et al. (2007) is less trivial due to the very different methodology. In that paper, they model the strong and stacked weak lensing signals for SLACS lenses jointly using the sum of an uncontracted NFW and a stellar Hernquist profile with a free M_*/L (without

any stellar mass estimates from stellar population synthesis methods). With this procedure, they quote a 3d stellar mass fraction within the effective radius of $f_* = 0.73$ (independent of h because of how the modeling is done). However, Jiang & Kochanek (2007) model the same SLACS sample, and find that if they allow for the possibility of adiabatic contraction, the resulting M_*/L is 70 per cent of the value when adiabatic contraction is ignored (see their figure 6). This decrease results from a degeneracy in the fits: an uncontracted DM profile requires more mass to be attributed to stars than a contracted DM profile, in order to account for the total mass. Furthermore, they find that the fit with AC (and lower value of M_*/L) is preferred once they include the weak lensing in the modeling. Consequently, the Jiang & Kochanek (2007) results suggest that this value of f_* from Gavazzi et al. (2007) should be reduced to ~ 0.5 , which is higher than our values of 0.31–0.38, but not very significantly once the different sample selections (strong lensing versus optical) and redshift ranges are taken into account.

Finally, we compare against the results from Cappellari et al. (2006), who find that for 25 SAURON E/S0 galaxies, the assumption of a Kroupa IMF yields $f_* \sim 0.7$ (median value, independent of h). While this number is significantly higher than ours, the selection criteria and redshift range of the galaxies are significantly different, so it is difficult to derive any conclusions from this comparison.

4 CONCLUSIONS

We have combined weak lensing and velocity dispersion observations to study the dark matter profiles of elliptical galaxies from the SDSS. The radial profile of the weak lensing shear is consistent with that expected from an NFW halo profile. We have fit two NFW parameters to the weak lensing data (mass and concentration), and extrapolated the profile inward to smaller radii not accessible to weak gravitational lensing. We have deduced the dynamical mass at these smaller radii by measuring the velocity dispersion of the stars within the half light radius of the galaxy. We compare the measured dynamical mass to the extrapolation of the NFW profile, and find that there is a significant excess of mass in the interior. Using estimates of the stellar mass of the galaxy, and assuming that all non-stellar mass is dark matter, we find that the dark matter contribution to the dynamical mass is still far in excess of the NFW prediction. This result is in support of the model of adiabatic contraction (AC), which predicts that the cooling and condensation of baryonic material will deepen the gravitational potential well of the galaxy, and pull the dark matter towards the halo center. These results suggest that the effects of AC are stable to the subsequent bombardment of major and minor mergers suffered by these objects since the time their gas cooled.

We compare the observation to a theoretical model of adiabatic contraction (Gnedin et al. 2004) and find good agreement between the two. However, we acknowledge that systematic uncertainties in the determination of the stellar mass make it difficult to prove that the excess mass at the half light radius is indeed dark matter. An alternative interpretation may be that the excess mass is comprised of some other dark baryonic form, for example it may indicate an

IMF with more of the mass concentrated in dim, low mass stars relative to the Kroupa IMF used in our stellar mass estimates. In order to fully explain the observation without adiabatic contraction, the stellar masses would need to increase by a factor of two. A change of this magnitude in the stellar masses would be difficult to reconcile with recent results from the SAURON collaboration. They conclude that a 30 per cent increase in stellar mass (from masses obtained with the Kroupa IMF) is inconsistent with their dynamical data derived from integral-field spectroscopy.

Finally, we divide the sample of galaxies along the mean size-luminosity relation and show that the scatter from the mean relation is related to the underlying properties of the dark matter profile. We find that due to a higher baryon fraction with more of the baryons concentrated toward the center, the smaller/brighter subsample experiences more lasting effects of adiabatic contraction than the larger/dimmer subsample. If adiabatic contraction is not the explanation, the most likely alternative is different IMFs for the two subsamples. Also, we find that the two subsamples have comparable stellar masses but different halo masses, suggesting that stellar mass does not trace halo mass, possibly due to different formation histories that result in differing dark and stellar components (with larger halo mass being associated with a dimmer, less concentrated stellar component).

Ultimately, regardless of whether the excess mass is dark matter or baryonic, this set of observations indicates that the total mass at the half light radius far exceeds what would naively be expected from an NFW or Einasto profile. Contemporary models of galaxy formation and evolution must accommodate this relatively high ratio of dynamical mass in the interior to total halo mass in early type elliptical galaxies.

ACKNOWLEDGMENTS

The authors thank Glenn van de Ven, Scott Tremaine, and Charlie Conroy for inspiring and helpful conversations. NP thanks Pieter van Dokkum for useful discussions. A.E.S. is supported by the Corning Glassworks fellowship. R.M.'s work on this project was supported by NASA through Hubble Fellowship grant #HST-HF-01199.02-A, awarded by the Space Telescope Science Institute, which is operated by the Association of Universities for Research in Astronomy, Inc., for NASA, under contract NAS 5-26555.

Funding for the SDSS and SDSS-II has been provided by the Alfred P. Sloan Foundation, the Participating Institutions, the National Science Foundation, the U.S. Department of Energy, the National Aeronautics and Space Administration, the Japanese Monbukagakusho, the Max Planck Society, and the Higher Education Funding Council for England. The SDSS Web Site is <http://www.sdss.org/>.

The SDSS is managed by the Astrophysical Research Consortium for the Participating Institutions. The Participating Institutions are the American Museum of Natural History, Astrophysical Institute Potsdam, University of Basel, University of Cambridge, Case Western Reserve University, University of Chicago, Drexel University, Fermilab, the Institute for Advanced Study, the Japan Participation Group, Johns Hopkins University, the Joint Institute for Nuclear Astrophysics, the Kavli Institute for Particle As-

trophysics and Cosmology, the Korean Scientist Group, the Chinese Academy of Sciences (LAMOST), Los Alamos National Laboratory, the Max-Planck-Institute for Astronomy (MPIA), the Max-Planck-Institute for Astrophysics (MPA), New Mexico State University, Ohio State University, University of Pittsburgh, University of Portsmouth, Princeton University, the United States Naval Observatory, and the University of Washington.

REFERENCES

- Abadi M. G., Navarro J. F., Fardal M., Babul A., Steinmetz M., 2009, preprint (arXiv:0902.2477)
- Abazajian K. et al. 2003, *Astron. J.*, 126, 2081
- Abazajian K. et al. 2004, *Astron. J.*, 128, 502
- Abazajian K. et al. 2005, *Astron. J.*, 129, 1755
- Abazajian K. N. et al. 2009, *Astrophys. J. Supp.*, 182, 543
- Adelman-McCarthy J. K. et al. 2006, *Astrophys. J. Supp.*, 162, 38
- Adelman-McCarthy J. K. et al. 2007, *Astrophys. J. Supp.*, 172, 634
- Adelman-McCarthy J. K. et al. 2008, *Astrophys. J. Supp.*, 175, 297
- Bartelmann M., Schneider P., 2001, *Phys. Rep.*, 340, 291
- Bernstein G. M., Jarvis M., 2002, *Astron. J.*, 123, 583
- Blanton M. R. et al. 2005, *Astron. J.*, 129, 2562
- Blanton M. R., Roweis S., 2007, *Astron. J.*, 133, 734
- Blumenthal G. R., Faber S. M., Flores R., Primack J. R., 1986, *Astrophys. J.*, 301, 27
- Bradač M. et al. 2008, *Astrophys. J.*, 681, 187
- Cappellari M. et al. 2006, *Mon. Not. R. Astron. Soc.*, 366, 1126
- Cappellari M. et al. 2007, *Mon. Not. R. Astron. Soc.*, 379, 418
- Corless V. L., King L. J., Clowe D., 2009, *Mon. Not. R. Astron. Soc.*, 393, 1235
- Dahle H., Hannestad S., Sommer-Larsen J., 2003, *Astrophys. J. Lett.*, 588, L73
- de Zeeuw P. T. et al. 2002, *Mon. Not. R. Astron. Soc.*, 329, 513
- Eisenstein D. J. et al. 2001, *Astron. J.*, 122, 2267
- Finkbeiner D. P. et al. 2004, *Astron. J.*, 128, 2577
- Fukugita M., Ichikawa T., Gunn J. E., Doi M., Shimasaku K., Schneider D. P., 1996, *Astron. J.*, 111, 1748
- Fukugita M., Hogan C. J., Peebles P. J. E., 1998, *Astrophys. J.*, 503, 518
- Gao L., Loeb A., Peebles P. J. E., White S. D. M., Jenkins A., 2004, *Astrophys. J.*, 614, 17
- Gao L., Navarro J. F., Cole S., Frenk C. S., White S. D. M., Springel V., Jenkins A., Neto A. F., 2008, *Mon. Not. R. Astron. Soc.*, 387, 536
- Gavazzi R., Treu T., Rhodes J. D., Koopmans L. V. E., Bolton A. S., Burles S., Massey R. J., Moustakas L. A., 2007, *Astrophys. J.*, 667, 176
- Gnedin O. Y., Kravtsov A. V., Klypin A. A., Nagai D., 2004, *Astrophys. J.*, 616, 16
- Gunn J. E. et al. 1998, *Astron. J.*, 116, 3040
- Hernquist L., 1990, *Astrophys. J.*, 356, 359
- Hirata C., Seljak U., 2003, *Mon. Not. R. Astron. Soc.*, 343, 459

Hogg D. W., Finkbeiner D. P., Schlegel D. J., Gunn J. E., 2001, *Astron. J.*, 122, 2129

Ivezić Ž. et al. 2004, *Astronomische Nachrichten*, 325, 583

Jiang G., Kochanek C. S., 2007, *Astrophys. J.*, 671, 1568

Johansson P. H., Naab T., Ostriker J. P., 2009, *Astrophys. J. Lett.*, 697, L38

Kauffmann G. et al. 2003, *Mon. Not. R. Astron. Soc.*, 341, 33

Kneib J.-P. et al. 2003, *Astrophys. J.*, 598, 804

Kroupa P., 2001, *Mon. Not. R. Astron. Soc.*, 322, 231

Limousin M. et al. 2007, *Astrophys. J.*, 668, 643

Lupton R. H., Gunn J. E., Ivezić Z., Knapp G. R., Kent S., Yasuda N., 2001, in *ASP Conf. Ser. 238: Astronomical Data Analysis Software and Systems X*, pp. 269–278

Mandelbaum R., Hirata C. M., Seljak U., Guzik J., Padmanabhan N., Blake C., Blanton M. R., Lupton R., Brinkmann J., 2005a, *Mon. Not. R. Astron. Soc.*, 361, 1287

Mandelbaum R., Tasitsiomi A., Seljak U., Kravtsov A. V., Wechsler R. H., 2005b, *Mon. Not. R. Astron. Soc.*, 362, 1451

Mandelbaum R., Seljak U., Cool R. J., Blanton M., Hirata C. M., Brinkmann J., 2006, *Mon. Not. R. Astron. Soc.*, 372, 758

Mandelbaum R., Seljak U., Hirata C. M., 2008a, *Journal of Cosmology and Astro-Particle Physics*, 8, 6

Mandelbaum R. et al. 2008b, *Mon. Not. R. Astron. Soc.*, 386, 781

Merritt D., Navarro J. F., Ludlow A., Jenkins A., 2005, *Astrophys. J. Lett.*, 624, L85

Morganti R. et al. 2006, *Mon. Not. R. Astron. Soc.*, 371, 157

Naab T., Johansson P. H., Ostriker J. P., Efstathiou G., 2007, *Astrophys. J.*, 658, 710

—, 1997, *Astrophys. J.*, 490, 493

Navarro J. F. et al., 2004, *Mon. Not. R. Astron. Soc.*, 349, 1039

Oguri M. et al. 2009, *Astrophys. J.*, 699, 1038

Okabe N., Takada M., Umetsu K., Futamase T., Smith G. P., 2009, preprint (arXiv:0903.1103)

Padmanabhan N. et al. 2004, *New Astronomy*, 9, 329

Padmanabhan N. et al. 2008, *Astrophys. J.*, 674, 1217

Pier J. R., Munn J. A., Hindsley R. B., Hennessy G. S., Kent S. M., Lupton R. H., Ivezić Ž., 2003, *Astron. J.*, 125, 1559

Read J. I., Trentham N., 2005, *Royal Society of London Philosophical Transactions Series A*, 363, 2693

Reid B. A., Spergel D. N., 2009, *Astrophys. J.*, 698, 143

Richards G. T. et al. 2002, *Astron. J.*, 123, 2945

Riemer-Sørensen S., Paraficz D., Ferreira D. D. M., Pedersen K., Limousin M., Dahle H., 2009, *Astrophys. J.*, 693, 1570

Rudd D. H., Zentner A. R., Kravtsov A. V., 2008, *Astrophys. J.*, 672, 19

Salpeter E. E., 1955, *Astrophys. J.*, 121, 161

Schlegel D. J., Finkbeiner D. P., Davis M., 1998, *Astrophys. J.*, 500, 525

Shimasaku K. et al. 2001, *Astron. J.*, 122, 1238

Smith J. A. et al. 2002, *Astron. J.*, 123, 2121

Stoughton C. et al. 2002, *Astron. J.*, 123, 485

Strauss M. A. et al. 2002, *Astron. J.*, 124, 1810

Tucker D. L. et al. 2006, *Astronomische Nachrichten*, 327,

821

Umetsu K. et al. 2009, *Astrophys. J.*, 694, 1643York D. G. et al. 2000, *Astron. J.*, 120, 1579

APPENDIX A: COMPUTATION OF THE WEAK LENSING SIGNAL

We compute the lensing signal in logarithmic radial bins from $30 h_{70}^{-1} \text{kpc}$ to $2.9 h_{70}^{-1} \text{Mpc}$ as a weighted summation over lens-source pairs in the bin, using the following estimator:

$$\Delta\Sigma(R) = \frac{\sum_{ls} w_{ls} \gamma_t^{(ls)} \Sigma_c^{(ls)}}{2\mathcal{R} \sum_{ls} w_{ls}}. \quad (\text{A1})$$

where the factor of $2\mathcal{R}$ arises due to the response of our ellipticity definition to a shear. \mathcal{R} , known as the “shear responsivity,” is approximately $1 - e_{\text{rms}}^2 \approx 0.87$ (Bernstein & Jarvis 2002).

The weight factors w_{ls} assigned to each pair include redshift information and the error on the source shape measurement via

$$w_{ls} = \frac{\Sigma_c^{-2}}{\sigma_e^2 + \sigma_{\text{SN}}^2}. \quad (\text{A2})$$

where σ_{SN}^2 , the intrinsic shape noise, was determined as a function of magnitude in Mandelbaum et al. (2005a), fig. 3. The factor of Σ_c^{-2} downweights pairs that are close in redshift, so that we are weighting by the inverse variance of $\Delta\Sigma$.

The critical surface density, Σ_c , is computed in two different ways, depending on the source sample. For sources with $r < 21$, we use photometric redshifts, and require that the source photometric redshift be greater than the lens redshift plus 0.1. The procedure for correcting these Σ_c estimates to account for photometric redshift error is described in Mandelbaum et al. (2005a, 2008b). For sources with $r > 21$, we use a redshift distribution for the sources, so that for a given lens redshift a single Σ_c value is used for all sources at $r > 21$. Finally, for the high-redshift LRG source sample used only at transverse separations $< 140 h_{70}^{-1} \text{kpc}$, we use photometric redshifts to assign Σ_c for each lens-source pair.

There are several additional procedures that must be done when computing the signal (for more detail, see Mandelbaum et al. 2005a). First, the signal computed around random points must be subtracted from the signal around real lenses to eliminate contributions from systematic shear. In practice, this correction is negligible on the scales used for this measurement. Second, the signal must be boosted, i.e. multiplied by $B(R) = n(R)/n_{\text{rand}}(R)$, the ratio of the number density of sources around real lenses relative to their number density around random points, in order to account for dilution by sources that are physically associated with lenses, and therefore not lensed.

In order to determine errors on the lensing signal, we divide the survey area into 200 bootstrap subregions, and generate 1000 bootstrap-resampled datasets.